



# High-Temperature Oxidation Behavior of NiCoCrAlY Coatings Deposited by Laser Cladding on 304 Stainless Steel

Yuxin Li<sup>1</sup> · Jinhao Nie<sup>1</sup> · Yixin Yang<sup>1</sup> · Peikang Bai<sup>1</sup> · Hongjian Zhang<sup>1</sup> · Zhanyong Zhao<sup>1</sup> · Shouzheng Wei<sup>1</sup> · Jie Cai<sup>2,3</sup> · Qingfeng Guan<sup>4</sup>

Received: 2 September 2020 / Accepted: 16 November 2020 / Published online: 19 January 2021  
© The Korean Institute of Metals and Materials 2021

## Abstract

To improve the high-temperature resistance of the key hot-end parts of the steam turbine, NiCoCrAlY coatings were deposited on a 304 stainless steel substrate by laser cladding. The microstructure and high-temperature oxidation behavior of the NiCoCrAlY coatings were analyzed. The results showed that the NiCoCrAlY coatings contained  $\gamma/\gamma'$  and  $\beta$  phases, and the microstructure was mainly composed of elongated columnar crystals. In addition, after 100 h of oxidation at three different oxidation temperatures (750, 850 and 950 °C), the coatings showed a relatively low oxidation rate, which was approximately a quarter of the oxidation rate of the substrate. At the same time, the protective  $\text{Cr}_2\text{O}_3$  scales were formed on the coating surface. When the oxidation temperature was 850 °C, the  $\text{FeCr}_2\text{O}_4$  spinel formed and internal oxidation zone appeared, when the oxidation temperature reached 950 °C, the  $\text{FeCr}_2\text{O}_4$  spinel gathered in the local area on the surface of the  $\text{Cr}_2\text{O}_3$  scale and the internal oxidation was aggravated. In other words, as the oxidation temperature increased, the Fe element in the matrix formed the  $\text{FeCr}_2\text{O}_4$  spinel, which accelerated the consumption of Cr element in the coatings and reduced the overall oxidation resistance of the NiCoCrAlY coatings.

**Keywords** Laser cladding · NiCoCrAlY coatings · Microstructure · Oxidation behavior

## 1 Introduction

Currently, coal-fired power generation still occupies an important and irreplaceable position in the world. Improving the thermal efficiency of steam turbines during coal-fired power generation and reducing the energy consumption and harmful gas emissions have become important issues to be solved. The steam temperature of ultra-supercritical steam turbines usually exceeds 600 °C, which obviously places

stringent requirements on the performance of high-strength heat-resistant stainless steel, which is a key component of steam turbines [1]. Therefore, it is a simple and effective method to prepare heat insulation or protective coating on its surface [2, 3]. Thermal insulation coatings can effectively reduce the temperature of hot-end components, and the protective coating has excellent resistance to high-temperature oxidation, thermal corrosion, wear resistance and sealing. Thermal insulation coatings have been widely used in aero-engines and other fields. They are expected to improve the efficiency of steam turbines and the high-temperature resistance of key-hot end components in steam turbines, such as blades, valves, and boiler pipes, to extend the service life. MCrAlY (M is transition group metal Ni or Co or a mixture of them) alloy coatings have good adhesion, a high modulus, a high strength and excellent high-temperature oxidation and corrosion resistance [4]; these materials can not only be used as a heat barrier layer (thermal barrier-coatings (TBCs)) on the substrate and ceramic surface layer of the combination layer but can also be used in many protective coatings for high-temperature alloy components [5, 6].

✉ Yuxin Li  
liyuxin@nuc.edu.cn

✉ Peikang Bai  
jinhaon@hotmail.com

<sup>1</sup> School of Materials Science and Engineering, North University of China, Taiyuan 030051, China

<sup>2</sup> Institute of Advanced Manufacturing and Modern Equipment Technology, Jiangsu University, Zhenjiang 212013, China

<sup>3</sup> School of Mechanical Engineering, Jiangsu University, Zhenjiang 212013, China

<sup>4</sup> School of Materials Science and Engineering, Jiangsu University, Zhenjiang 212013, China

At present, atmospheric plasma spraying (APS) [7], high-velocity oxy-fuel (HVOF) [8], low-pressure plasma sputtering [9], and electron beam physical vapor deposition [10] are the most important preparation methods for MCrAlY coatings. However, regardless of which of the above methods are used, there are problems with the coatings, such as poor density and easy oxidation [11], which obviously have a very adverse effect on the high-temperature oxidation and corrosion performance of the coating. The research results show that oxide impurities in the coating increase the growth rate of TGO, which leads to early failure of the coating [12, 13]. For example, due to high-temperature sputtering techniques, including APS and HVOF, oxide impurities are inevitably formed during the deposition process, while low-pressure plasma sputtering and vacuum plasma sputtering techniques can effectively avoid oxidation during the deposition process, but their cost is high. In contrast, laser cladding under the protection of an inert gas contributes to solving the above problems. It can prepare a metal coating with a dense and fine structure that metallurgically combines with the substrate and reduces the internal and surface coating defects [14–17], which effectively blocks the diffusion of oxygen into the coating in a high-temperature environment [18, 19].

In the present study, a NiCoCrAlY coating was prepared on the surface of 304 stainless steel by laser cladding. First, the microstructure of the NiCoCrAlY coating was studied, and then isothermal oxidation experiments were carried out at 750 °C, 850 °C, and 950 °C. The oxidation kinetics of the 304 stainless steel before and after LC were compared. The morphology of the oxide layer was observed, in order to evaluate their evolution with oxidation temperature. By analyzing the concentration of elements after oxidation, we focused on determining the antioxidation mechanism of the NiCoCrAlY coating prepared by laser cladding, which provides a theoretical reference for the application of NiCoCrAlY coating.

## 2 Experimental Procedures

### 2.1 Preparation of the Samples

In this research, the substrate comprised 304 stainless steel with a size of 20 mm × 20 mm × 10 mm. The chemical composition is given in Table 1. The cladding powder comprised NiCoCrAlY, and the chemical composition is shown in Table 2. The scanning electron microscope (SEM, S-3400 N HITACHI) image of NiCoCrAlY powder particles is shown

**Table 1** Chemical composition of 304 stainless steel

Element	C	Si	Mn	P	S	Cr	Ni	Fe
wt%	0.040	0.378	0.903	0.040	0.004	18.330	8.110	Bal.

**Table 2** Chemical composition of NiCoCrAlY

Element	Co	Cr	Al	Y	Ni
wt%	22.88	17.96	11.82	0.99	Bal.

in Fig. 1a. The particle size distribution was measured using a laser particle size analyzer (Mastersizer.2000). The particle size distribution diagram is shown in Fig. 1b, where D10 = 38.42 μm, D50 = 68.75 μm, D90 = 123.28 μm. Before laser cladding, the surface of the substrate was mechanically polished and then cleaned with absolute ethanol to eliminate residual oils, oxides or other impurities.

The working principle of the laser cladding system is illustrated in Fig. 2. The powder was transported to the surface of the substrate through a powder feeding system (DMS-3). At the same time, it was scanned and deposited on the substrate by a laser (LDF4000-100, continuous wave with a wavelength from 980 to 1020 nm, Germany) to form a cladding layer. After a detailed study of the laser cladding parameters, they were selected as follows: the laser power was 1500 W, scanning speed was 10 mm/s, laser radius was 4 mm, overlap rate was 50%, and powder feed rate was 4500 mg/min. Argon gas was used as the protective and powder carrier gas, and the flow rate was 20 L/min. After laser cladding, the sample was cooled to room temperature in air.

### 2.2 Microscopic Analysis

The phase analysis of the NiCoCrAlY powder and NiCoCrAlY coating was carried out by X-ray diffraction (XRD, D/Max 2500PC, Japan). To eliminate the adverse effect of the relatively rough coating surface on the final result, the coating surface was ground and polished with sandpaper before the XRD analysis. Scanning electron microscopy (SEM FEI NovaNano450) and energy dispersive spectroscopy (EDS) were used to observe the microstructure of the NiCoCrAlY coating. Before observation, the coating section was polished and then etched with aqua regia for 30 s.

### 2.3 High-Temperature Oxidation Testing of the Coating

The 304 stainless steel was oxidized in a medium- and high-temperature (500–800 °C) environment. When the temperature is higher than 800 °C, the oxidation becomes severe. Therefore, the high-temperature oxidation behavior tests

**Fig. 1** SEM image (a) and particle size distribution (b) of NiCoCrAlY powder

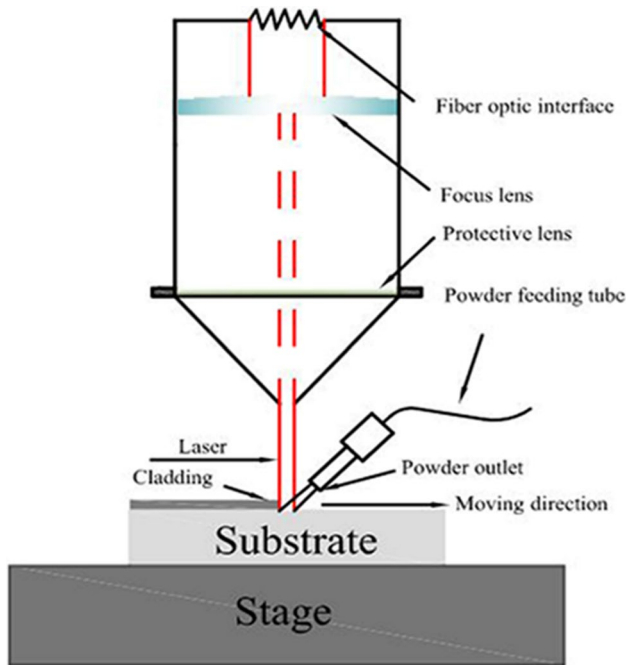
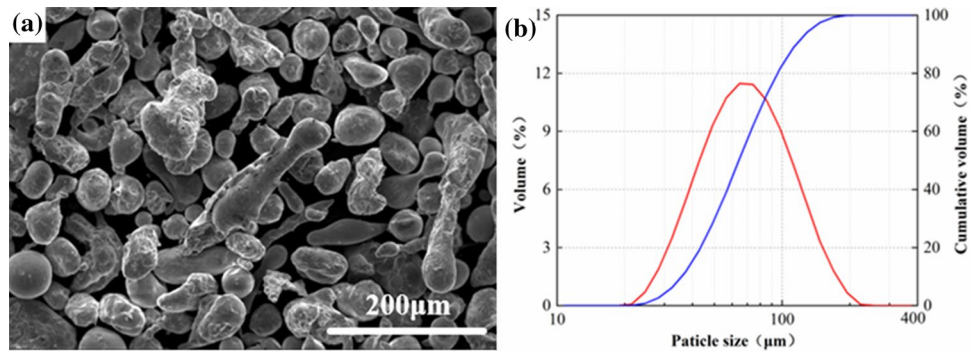


**Fig. 2** The working principle of laser cladding system

were carried out in a box-type resistance furnace at 750 °C, 850 °C, and 950 °C. The coated and uncoated substrates were subjected to isothermal oxidation for 100 h. During the experiment, the weight of the samples was measured using an electronic balance with a sensitivity of 0.1 mg every 10 h. After weighing, the samples were returned to the furnace to continue the remaining oxidation process. To ensure the accuracy of the outcome, the crucible was weighed before the experiment, and the samples were weighed together with the crucible during the experiment. The weight gain of the coating and substrate per unit area was calculated. The phase composition of the coating surface after oxidation was analyzed using X-ray diffraction. The surface morphology and cross-sectional morphology of the oxide film were observed with scanning electron microscopy. The composition of the oxides was determined by energy dispersive spectrometry (EDS).

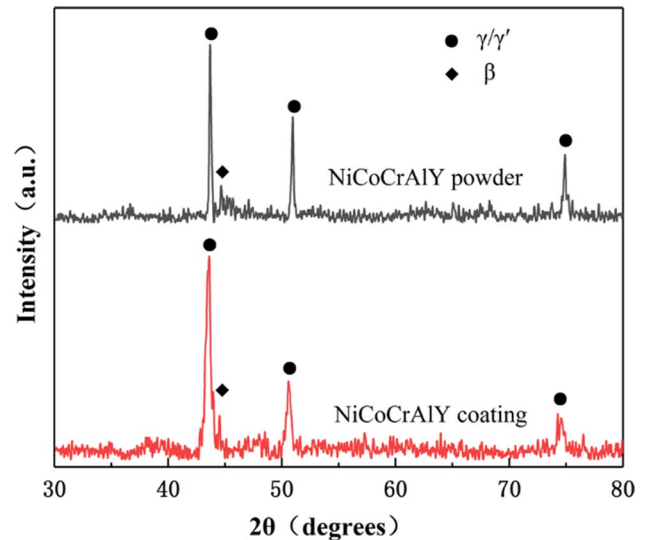


**Fig. 3** XRD patterns of the NiCoCrAlY powder and NiCoCrAlY coating

## 3 Results and Discussion

### 3.1 Microstructure of the Coatings

Figure 3 gives the results of the XRD analyses of the NiCoCrAlY powder and NiCoCrAlY coating. The NiCoCrAlY powder before cladding and the NiCoCrAlY coating after cladding are composed of γ/γ' and β phases. The half-widths of the three strong peaks in the XRD pattern of the powder are 0.3648, 0.3192, and 0.3534, respectively, and the half-widths of the three strong peaks in the XRD pattern of the coating are 0.6726, 0.6635, and 0.8208, respectively. We can clearly see that the diffraction peak of the coating is wider than that of NiCoCrAlY powder, which can be inferred that the grains become smaller after cladding [20–22]. The reason for this phenomenon may be that the cooling rate after laser cladding is too large, and the grains cannot grow.

Figure 4 presents the macroscopic and microscopic morphologies of the coating. From the macroscopic

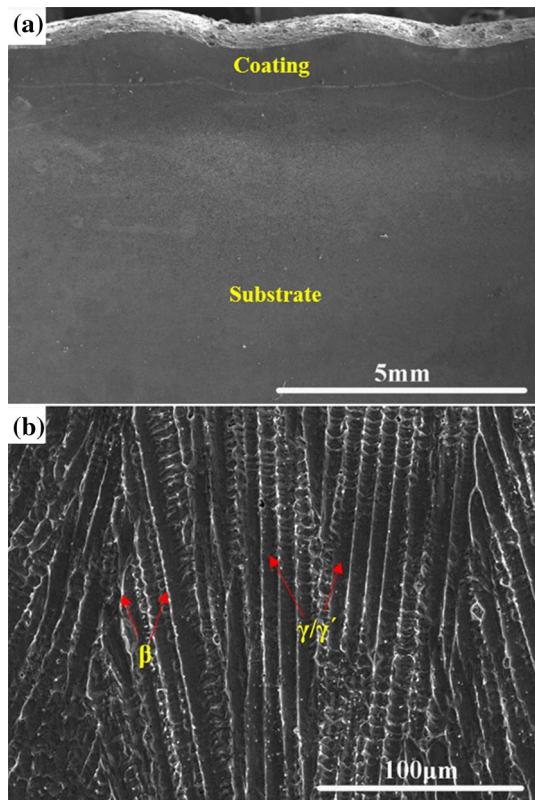


**Fig. 4** The cross-sectional morphology of the NiCoCrAlY coating: **a** macroscopic morphology, **b** microscopic morphology

morphology (Fig. 4a), it can be seen that the thickness of the coating is approximately 917  $\mu\text{m}$ , and no obvious cracks or pores are found. The microstructure of the coating (Fig. 4b) is mainly composed of many elongated columnar dendrites. This is the typical structure produced by a laser as the heat source under the conditions of rapid heat and rapid cooling, which greatly reduces the oxidation channels of metal elements compared to that of the polycrystalline structure. The dark area corresponds to the Al-poor  $\gamma/\gamma'$  phase, and the bright area corresponds to the Al-rich  $\beta$  phase. These two phases are also confirmed by the XRD analysis. The  $\beta$  phase exhibits a dendritic microstructure with a high aspect ratio. This structure enables the exclusive formation of alumina and a lower thermally grown oxide (TGO) growth rate [23].

### 3.2 Oxidation Behavior

Figure 5 shows the quality change of the coating and substrate after oxidation. After 100 h of oxidation, the weight gain of the substrate increases rapidly from 2.7219 to 4.5631  $\text{mg}/\text{cm}^2$ , while the weight gain of the NiCoCrAlY coating increases from 0.91667 to 1.3501  $\text{mg}/\text{cm}^2$ . The

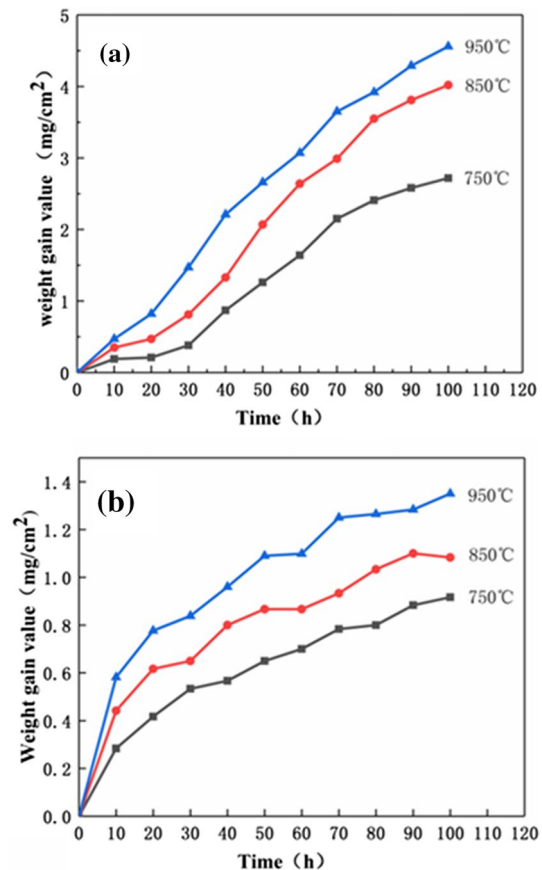


**Fig. 5** The weight gain value of the 304 stainless steel **(a)** and the NiCoCrAlY coating **(b)** at 750, 850, and 950  $^{\circ}\text{C}$

growth is slow, and the coating has better oxidation resistance than the substrate.

According to the weight gain from oxidation as a function of the time, it can be seen that the weight increase of the substrate has a linear relationship with the time (Fig. 5a). However, the weight gain of the NiCoCrAlY coating has an exponential relationship with the time (Fig. 5b), which is consistent with Wagner's oxidation theory [24–26]. According to Wagner's theory, the weight change due to oxidation can be expressed by Eq. (1):

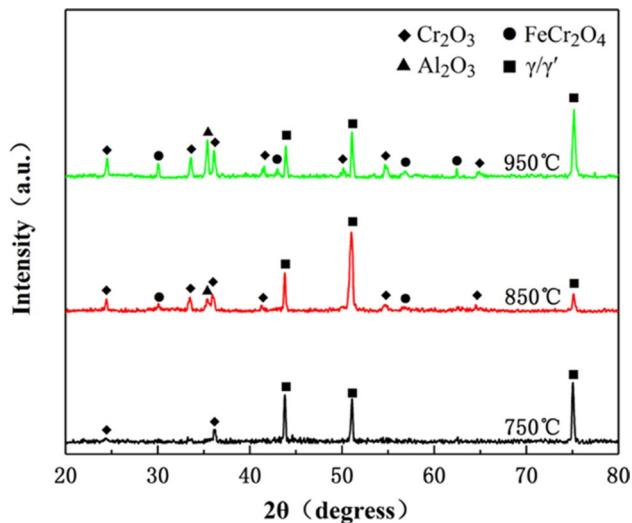
$$(\Delta W)^n = At \quad (1)$$

where  $\Delta W$  is the weight increase,  $n$  is the oxidation index,  $A$  is a constant (oxidation rate), and  $t$  is the oxidation time. Table 3 lists the fitting equations for the 304 stainless steel substrate and NiCoCrAlY coating. For the NiCoCrAlY coating, the oxidation index is 2, which indicates that the diffusion of oxidation is affected not only by the diffusion behavior of oxygen but also by the surface chemical reaction [27]. The oxidation rate (curve slope) of the substrate at 750, 850, and 950  $^{\circ}\text{C}$  is 0.03256, 0.04585, and 0.04829, respectively,



**Table 3** Parameters of oxidation models fitted to weight gain data of the 304 stainless steel alloy and the NiCoCrAlY coatings

Materials	Equation	Time(h)
<i>304 stainless steel</i>		
750 °C	$\Delta W = 0.03256t - 0.35$	10–100
850 °C	$\Delta W = 0.04585t - 0.318$	10–100
950 °C	$\Delta W = 0.04829t + 0.076$	10–100
<i>NiCoCrAlY coating</i>		
750 °C	$(\Delta W)^2 = 0.00838t$	10–100
850 °C	$(\Delta W)^2 = 0.01142t$	10–100
950 °C	$(\Delta W)^2 = 0.01696t$	10–100

**Fig. 6** XRD patterns of the NiCoCrAlY coating after 100 h of oxidation at different temperatures

and the oxidation rate of the NiCoCrAlY coating is 0.00838, 0.01142, and 0.01696, respectively. According to the oxidation rate constant (A), it can be concluded that the oxidation rate of the coating is approximately a quarter of the oxidation rate of the substrate. When these results are combined with the oxidative weight gain of the coating, it appears that the coating has excellent antioxidation properties.

Figure 6 displays the XRD analysis results after isothermal (750, 850 and 950 °C) oxidation for 100 h. After oxidation at 750 °C, the coating surface contains  $\gamma/\gamma'$  and  $\text{Cr}_2\text{O}_3$  phases. The  $\text{Cr}_2\text{O}_3$  phase prevents further oxidation of the coating [28]. The  $\text{FeCr}_2\text{O}_4$  phase and  $\text{Al}_2\text{O}_3$  phase appear after oxidation at 850 °C. During the laser cladding process, a small amount of matrix elements (Fe) diffuse into the coating [29]. Since Fe has a higher activity than Ni and Co, it forms the  $\text{FeCr}_2\text{O}_4$  phase. The high density of the  $\text{Al}_2\text{O}_3$  phase has a better ability to isolate oxygen than the  $\text{Cr}_2\text{O}_3$  phase [27]. With increasing oxidation temperature, the peaks from the  $\text{Cr}_2\text{O}_3$  phase and  $\text{Al}_2\text{O}_3$  phase increase at

950 °C, indicating that more  $\text{Cr}_2\text{O}_3$  phase and  $\text{Al}_2\text{O}_3$  phase are formed on the coating surface.

Figure 7 shows the micromorphology of the NiCoCrAlY coating surface after oxidation at different temperatures for 100 h. After oxidizing at 750 °C for 100 h (Fig. 7a, b), the surface of the coating is divided into planar areas and river-like areas. The surface of the planar area is composed of a large number of particulate oxidation products. The size of the oxidation products deposited on the coating is small, and the structure is dense, which can effectively restrict the number of oxygen diffusion channels. The EDS results (Table 4) show that the main component in the planar area (Point 1) is  $\text{Cr}_2\text{O}_3$ , which is the result of selective oxidation in a high-temperature environment. The dense  $\text{Cr}_2\text{O}_3$  scale isolates the internal regions from the oxidizing environment. In the river-like area (Point 2), the Al element content (13.07 at%) is significantly higher than that in the planar area (1.14 at%). It can be speculated that the coating in this area contains a small amount of alumina in addition to  $\text{Cr}_2\text{O}_3$ . However, alumina is not detected by X-ray diffraction. The main reason is that the size and quantity of the alumina are very small; it is difficult to determine the alumina phase composition by X-ray diffraction [30].

When the temperature is 850 °C (Fig. 7c, d), the coating surface is stacked with oxidation products that have a polyhedral structure and granular structure. The surface structure appears less dense. The polyhedral-like oxidation products (Point 3) are  $\text{FeCr}_2\text{O}_4$  spinel, and the granular oxides (Point 4) are  $\text{Cr}_2\text{O}_3$ . The spinel is doped with  $\text{Cr}_2\text{O}_3$ . Compared with that at 750 °C, the  $\text{Cr}_2\text{O}_3$  particle size increases, indicating that  $\text{Cr}_2\text{O}_3$  gradually grows as the temperature increases.

When the temperature is 950 °C (Fig. 7e–g), the surface morphology changes substantially. The flocculated oxidation products are formed, and local areas are also covered with the polyhedron-like oxidation products. There are obvious holes and cracks in the flocculated oxidation products, some of the flocculated oxidation products are peeled off, and a new scale layer appears. The new scale layer (Fig. 7g) is composed of stacked particles, and its surface structure is flat and dense. According to EDS analysis, the polyhedral oxidation product (Point 5) is  $\text{FeCr}_2\text{O}_4$  spinel, the flocculated oxidation product (Point 6) is  $\text{Cr}_2\text{O}_3$ , and the new scale layer (Point 7) is rich in Al and O, indicating that the scale is alumina. For the new scale layer that appears on the surface after shedding, it is difficult to identify whether this  $\text{Al}_2\text{O}_3$  scale was newly formed or already existed underneath the spalled scale based on the surface morphology.

Figure 8 shows the cross-sectional morphology of the samples and the corresponding EDS results for the local area after oxidation at 750, 850, and 950 °C for 100 h. From the surface of the coating to the inside of the coating, the contents of Ni, Co, and Fe gradually increase (Fig. 8d–f),

**Fig. 7** Surface morphology of the NiCoCrAlY coating after 100 h of oxidation at different temperatures: **a, b** 750 °C, **c, d** 850 °C, **e–g** 950 °C

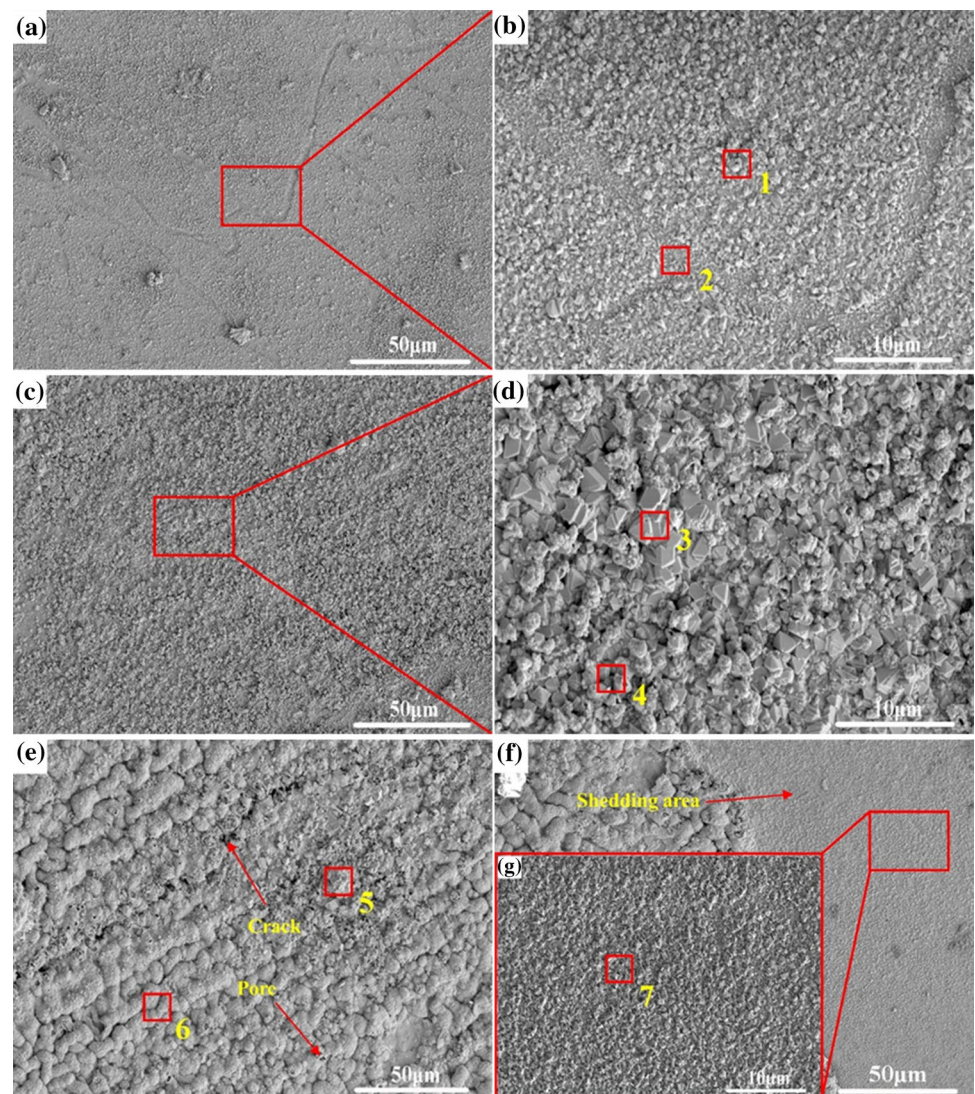


**Table 4** EDS results at each point marked in Fig. 7 (at%)

EDS point	Composition (at%)						
	O	Al	Cr	Fe	Ni	Co	Y
1	44.61	1.14	39.22	1.93	5.84	7.26	–
2	33.61	13.07	27.32	8.05	8.21	9.74	–
3	58.21	2.03	26.5	11.32	1.57	0.37	–
4	54.62	1.22	40.99	1.92	0.47	0.77	0.01
5	57.35	0.54	29.31	12.13	0.27	0.4	–
6	59.11	0.23	36.22	2.26	1.26	0.91	0.01
7	51.82	32.81	10.62	1.85	1.31	1.59	–

indicating that the elements of Ni, Co, and Fe are consumed by the scale during the early oxidation process [27]. At 750 °C (Fig. 8a), a continuous dense oxide layer is observed on the surface of the coating. The EDS results (Fig. 8d) show that the main component of the oxide film is  $\text{Cr}_2\text{O}_3$ , and the content of Al increases slightly, indicating that the

oxide layer also contains a small amount of  $\text{Al}_2\text{O}_3$ , which is consistent with the surface observation results. At 850 °C (Fig. 8b), in addition to the oxide film, an internal oxidation zone appears. The oxide film shows a typical double-layer structure, and combined with the EDS result (Fig. 8e) and surface morphology, the upper layer of the oxide film



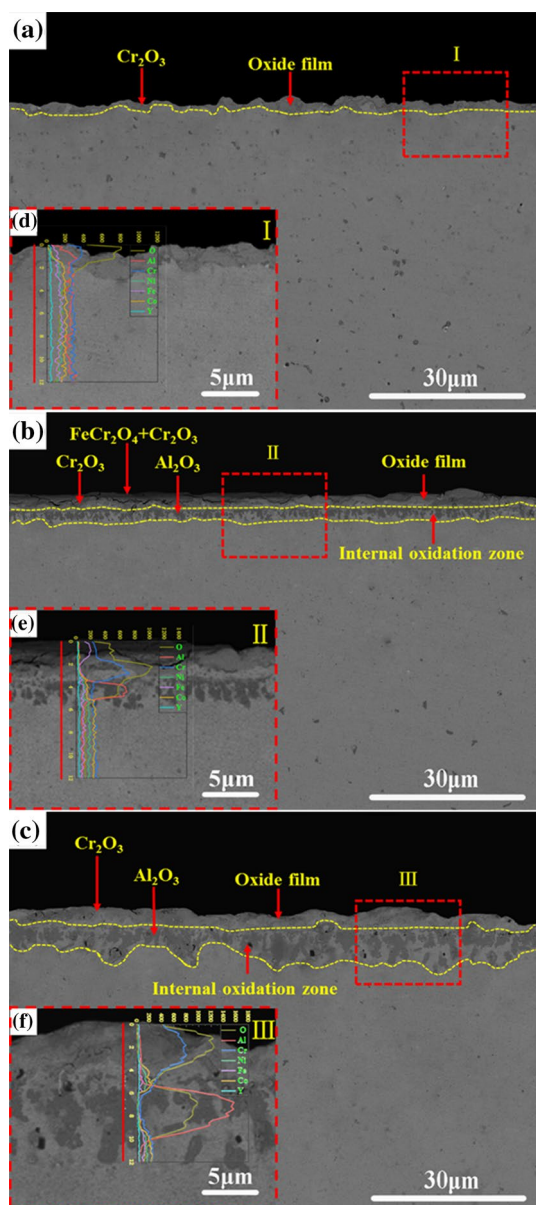


**Fig. 8** The cross-sectional BSE morphology and EDS line analysis of the NiCoCrAlY coating after 100 h of oxidation at different temperatures: **a** low-magnified image at 750 °C, **b** low-magnified image at 850 °C, **c** low-magnified image at 950 °C, **d–f** high-magnified image and EDS line analysis showing the oxide scale

is a mixture of  $\text{FeCr}_2\text{O}_4$  spinel and  $\text{Cr}_2\text{O}_3$ . Due to the different thermal expansion coefficients of the  $\text{FeCr}_2\text{O}_4$  spinel and  $\text{Cr}_2\text{O}_3$ , which form a growth stress, obvious cracks appear [31, 32]. The lower layer of the oxide film is  $\text{Cr}_2\text{O}_3$ . Combined with the surface morphology, it can be seen that the gap between the  $\text{Cr}_2\text{O}_3$  particles is large and the structure is loose. The thickness of the internal oxidation zone is approximately 2.05  $\mu\text{m}$ , and the oxidation products are mainly  $\text{Al}_2\text{O}_3$ . The O enters the interior by the gap between  $\text{Cr}_2\text{O}_3$  particles and combines with Al to form the oxidation

products [28]. As the oxidation process progresses, the  $\text{Al}_2\text{O}_3$  grows and aggregates, forming an internal oxide layer. The  $\text{Al}_2\text{O}_3$  is discontinuous, which is also a typical feature of internal oxidation. At 950 °C (Fig. 8c), the oxide film fluctuates greatly, and the internal oxidation zone becomes thick. Combined with the EDS result (Fig. 8f), it can be seen that the oxide film is  $\text{Cr}_2\text{O}_3$ . It can be found that the Cr element concentration near the oxide film reaches its lowest value, indicating that the Cr content is already low and can no longer generate new  $\text{Cr}_2\text{O}_3$ , which is the direct cause of the pores, cracks and shedding phenomena that occur on the  $\text{Cr}_2\text{O}_3$  scale. The thickness of the internal oxide zone is approximately 5.85  $\mu\text{m}$ , indicating that the ability of the  $\text{Cr}_2\text{O}_3$  to isolate oxygen is weakened and additional O enters the interior of the coating. The composition of the internal oxidation zone is  $\text{Al}_2\text{O}_3$ , and the discontinuity of the  $\text{Al}_2\text{O}_3$  is more obvious than that at 850 °C. According to the EDS results (Fig. 8f), in the non- $\text{Al}_2\text{O}_3$  area of the internal oxidation zone, the O element content rapidly decreases, indicating that Al preferentially combines with O to form  $\text{Al}_2\text{O}_3$ , and the Al element protects other elements from being oxidized.

Therefore, the high-temperature oxidation behavior of the NiCoCrAlY coating at different temperatures can be described by the steps shown in Fig. 9. The antioxidation mechanism of the NiCoCrAlY coating is based on the formation of protective oxidation products, such as  $\text{Al}_2\text{O}_3$  and  $\text{Cr}_2\text{O}_3$ . During the initial stage of oxidation, due to the rapid weight gain, it can be speculated that all the elements (Ni, Co, Cr, Al, and Fe) exposed to a high-temperature environment are oxidized while the resulting mixed oxides are formed on the surface. As the oxidation proceeds, the selective oxidation of Cr is advantageous due to its high content, whereas the diffusion of Al is weakened or delayed [33]. After oxidizing at 750 °C for 100 h, the Cr element uses the grain boundaries as a diffusion channel and preferentially oxidizes to form  $\text{Cr}_2\text{O}_3$ ; also, a small amount of  $\text{Al}_2\text{O}_3$  is mixed in the  $\text{Cr}_2\text{O}_3$  oxidation product. At this temperature, the NiCoCrAlY coating exhibits excellent oxidation resistance. At 850 °C, the  $\text{FeCr}_2\text{O}_4$  spinel appears, which is doped with  $\text{Cr}_2\text{O}_3$  on the surface of the TGO layer, forming a mixed oxide scale. The mixed oxide scale contains obvious cracks and shedding. Below the mixed scale is a less dense  $\text{Cr}_2\text{O}_3$  scale. The O element enters the interior through the gaps between the  $\text{Cr}_2\text{O}_3$  particles. Al begins to oxidize selectively and gradually forms a less continuous  $\text{Al}_2\text{O}_3$ . When the temperature is 950 °C, the  $\text{FeCr}_2\text{O}_4$  spinel gathers in the local area on the surface of the  $\text{Cr}_2\text{O}_3$  scale. Cr consumption is accelerated and becomes depleted; thus, it is unable to generate new  $\text{Cr}_2\text{O}_3$ . The  $\text{Cr}_2\text{O}_3$  scale is severely damaged, and defects such as pores, cracks, and shedding appear. Additional oxygen enters the interior through the cracks and pores, and additional  $\text{Al}_2\text{O}_3$  is generated. The thickness of

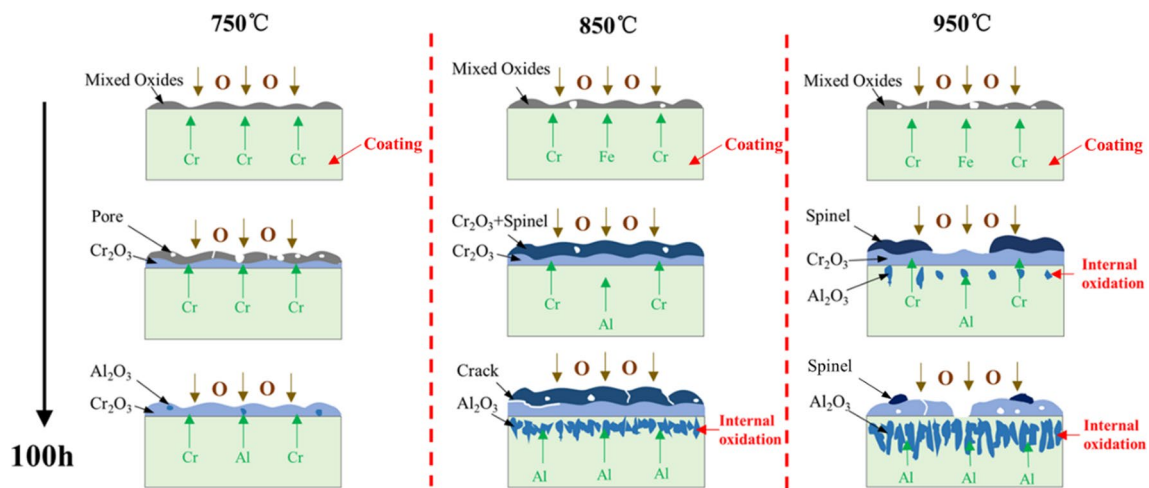


**Fig. 9** Schematic illustration of high-temperature oxidation processes of the NiCoCrAlY coating

the Al<sub>2</sub>O<sub>3</sub> scale increases, and the discontinuities become very obvious. In short, the matrix element (Fe) diffused into the coating during the laser cladding process has a certain effect on the oxidation resistance of the coating. Due to the higher activity of Fe element and the faster diffusion rate, FeCr<sub>2</sub>O<sub>4</sub> spinel is formed. The FeCr<sub>2</sub>O<sub>4</sub> spinel will consume the protective Cr<sub>2</sub>O<sub>3</sub> and accelerate the consumption of Cr element. Therefore, it can be said that the 304 stainless steel matrix has a certain negative effect on the high temperature oxidation performance of the NiCoCrAlY coating.

## 4 Conclusions

In this study, a NiCoCrAlY coating was prepared on a 304 stainless steel substrate by laser cladding technology. The structure and oxidation behavior of the coating were studied. The conclusions are as follows:

1. The NiCoCrAlY powder and the NiCoCrAlY coating contain  $\gamma/\gamma'$  and  $\beta$  phases. The microstructure of the NiCoCrAlY coating is mainly composed of many elongated columnar dendrites.
2. The NiCoCrAlY coating has good oxidation resistance, and the oxidation rate of the coating is approximately a quarter of the oxidation rate of the substrate.
3. The NiCoCrAlY coating is oxidized for 100 h. At 750 °C, Cr<sub>2</sub>O<sub>3</sub> in the stable and dense TGO layer plays a predominant protective role. At 850 °C, the internal oxide layer appears. Cr<sub>2</sub>O<sub>3</sub> and Al<sub>2</sub>O<sub>3</sub> play a synergistic protective role. When the temperature is 950 °C, the Cr<sub>2</sub>O<sub>3</sub> scale is severely damaged, the thickness of the internal oxidation zone increases, and Al<sub>2</sub>O<sub>3</sub> controls the subsequent oxidation behavior.

**Acknowledgements** The authors would like to acknowledge Natural Science Foundation of China (No. U1810112) and Taiyuan Science and Technology Project (No. 170205) for the financial support.

**Data Availability** The raw/processed data required to reproduce these findings cannot be shared at this time as the data also forms part of an ongoing study.

## Compliance with Ethical Standards

**Conflict of interests** The authors declare that they have no known competing financial interests or personal relationships that could have appeared to influence the work reported in this paper.

## References

1. H. Wärner, M. Calmunger, G. Chai, J. Polák, R. Petráš, M. Heczko, T. Kruml, S. Johansson, J. Moverare, *Procedia Struct. Integr.* **13**, 843–848 (2018)
2. Q.Z. Cui, S.M. Seo, Y.S. Yoo, Z. Lu, S.W. Myoung, Y.G. Jung, U. Paik, *Surf. Coat. Technol.* **284**, 69–74 (2015)
3. W. Uczak de Goes, N. Markocsan, M. Gupta, R. Vaßen, T. Matsushita, K. Illkova, *Surf. Coat. Technol.* **396**, 125950 (2020)
4. V.K. Tolpygo, D.R. Clarke, *Acta Mater.* **52**, 5115–5127 (2004)
5. I. Gurrappa, A. SambasivaRao, *Surf. Coat. Technol.* **201**, 3016–3029 (2006)
6. U. Schulz, C. Leyens, K. Fritscher, M. Peters, B. Saruhan-Brings, O. Lavigne, J.M. Dorvaux, M. Poulain, R. Mévrel, M. Caliez, *Aerosp. Sci. Technol.* **7**, 73–80 (2003)
7. E. Hejrani, D. Sebold, W.J. Nowak, G. Mauer, D. Naumenko, R. Vaßen, W.J. Quadackers, *Surf. Coat. Technol.* **313**, 191–201 (2017)
8. A. Feizabadi, M. SalehiDoolabi, S.K. Sadrnezhad, M. Rezaei, *J. Alloys Compd.* **746**, 509–519 (2018)
9. B.Y. Zhang, G.J. Yang, C.X. Li, C.J. Li, *Appl. Surf. Sci.* **406**, 99–109 (2017)
10. Y.J. Xie, M.C. Wang, *Surf. Coat. Technol.* **201**, 3564–3570 (2006)
11. G. Mauer, M.O. Jarligo, D.E. Mack, R. Vaßen, *J. Therm. Spray Technol.* **22**, 646–658 (2013)



12. P. Song, D. Naumenko, R. Vassen, L. Singheiser, W.J. Quadackers, *Surf. Coat. Technol.* **221**, 207–213 (2013)
13. P. Richer, M. Yandouzi, L. Beauvais, B. Jodoin, *Surf. Coat. Technol.* **204**, 3962–3974 (2010)
14. C. Bezençon, A. Schnell, W. Kurz, *Scr. Mater.* **49**, 705–709 (2003)
15. Y.N. Wu, G. Zhang, Z.C. Feng, B.C. Zhang, Y. Liang, F.J. Liu, *Surf. Coat. Technol.* **138**, 56–60 (2001)
16. Y.X. Li, P.F. Zhang, P.K. Bai, L.Y. Wu, B. Liu, Z.Y. Zhao, *Surf. Coat. Technol.* **334**, 142–149 (2018)
17. Y.X. Li, K.Q. Su, P.K. Bai, L.Y. Wu, *Mater. Charact.* **159**, 110023 (2020)
18. J.C. Pereira, J.C. Zambrano, M.J. Tobar, A. Yañez, V. Amigó, *Surf. Coat. Technol.* **270**, 243–248 (2015)
19. K. Partes, C. Giolli, F. Borgioli, U. Bardi, T. Seefeld, F. Vollertsen, *Surf. Coat. Technol.* **202**, 2208–2213 (2008)
20. H.M. Wang, J.S. Jiang, Z.Y. Huang, Y. Chen, K. Liu, Z.W. Lu, J.Q. Qi, F. Li, D.W. He, T.C. Lu, Q.Y. Wang, *J. Alloys Compd.* **671**, 527–531 (2016)
21. N.M. Martyak, K. Drake, *J. Alloys Compd.* **312**, 30–40 (2000)
22. C. Kaplin, M. Brochu, *Appl. Surf. Sci.* **301**, 258–263 (2014)
23. L. Luo, H. Zhang, Y. Chen, C. Zhao, S. Alavi, F. Guo, X. Zhao, P. Xiao, *Corros. Sci.* **145**, 262–270 (2018)
24. H. Barekatin, S.M. MousaviKhoei, *Surf. Coat. Technol.* **384**, 125339 (2020)
25. C. Wagner, *Corros. Sci.* **9**, 91–109 (1969)
26. L.Z. Du, W.T. Zhang, W.G. Zhang, T.T. Zhang, H. Lan, C.B. Huang, *Surf. Coat. Technol.* **298**, 7–14 (2016)
27. S. Cui, Q. Miao, W. Liang, B. Li, *Appl. Surf. Sci.* **428**, 781–787 (2018)
28. H.J. Xie, Y.L. Cheng, S.X. Li, J.H. Cao, L. Cao, *Trans. Nonferrous Met. Soc. China (English Ed)* **27**, 336–351 (2017)
29. G. Moskal, D. Niemiec, B. Chmiela, P. Kałamarz, T. Durejko, M. Ziętała, T. Czujko, *Surf. Coat. Technol.* **387**, 125317 (2020)
30. J.J. Liang, Y.S. Liu, J.G. Li, Y.Z. Zhou, X.F. Sun, *J. Mater. Sci. Technol.* **35**, 344–350 (2019)
31. H. Peng, H.B. Guo, R. Yao, J. He, S.K. Gong, *Vacuum* **85**, 627–633 (2010)
32. A.H. Heuer, D.B. Hovis, J.L. Smialek, B. Gleeson, *J. Am. Ceram. Soc.* **94**, 2698 (2011)
33. J. Cai, C.Z. Gao, P. Lv, C.L. Zhang, Q.F. Guan, J.Z. Lu, X.J. Xu, *J. Alloys Compd.* **784**, 1221–1233 (2019)

**Publisher's Note** Springer Nature remains neutral with regard to jurisdictional claims in published maps and institutional affiliations.